ADVANCED OPTICAL MATERIALS
www.advopticalmat.de

Asymmetric Contacts on Narrow-Bandgap Black Phosphorus for Self-Driven Broadband Photodetectors

Kai Tang, Chaoyi Yan, Xinchuan Du, Gaofeng Rao, Miao Zhang, Yang Wang, Xianfu Wang,* and Jie Xiong**

Self-driven broadband photodetectors based on two-dimensional (2D) materials have attracted considerable interest for their outstanding optoelectronic properties. Asymmetric contact induced potential barrier on 2D narrow-bandgap materials is a feasible scheme for self-driven broadband photodetectors, but has not been constructed untill now due to the band structure mismatch of the channel and metal electrodes. Herein, a self-driven broadband photodetector is reported covering from visible to infrared spectrum by well designing the band structure of the Cr/BP/WTe_2 heterostructure with asymmetric contact architecture, constructing a huge potential barrier at the two ends of the black phosphorus (BP) channel due to the perfect ohmic and Schottky contacts at the WTe_2-BP and Cr-BP interfaces, respectively. The as-fabricated device exhibits responsivity of ∼283 and ∼193 mA/W under 532 and 1550 nm illumination, respectively, under zero bias with corresponding detectivity of $\sim 2.3\times10^{11}$ and $\sim 1.2\times10^{11}$ Jones. The results demonstrate that the well-designed band structure can be adopted to construct ideal Schottky and ohmic contact on 2D narrow-bandgap materials to realize a self-driven broadband photodetector. These findings highlight a simple and novel strategy for constructing predesigned band structure for further electronic and optoelectronic applications.

1. Introduction

As the key component in the optoelectronic integration system which including light emissions, optical waveguides, optoelectronic receivers and electronic circuits, high-performance photodetectors are regarded as the core of modern communication and imaging systems.[1] Particularly, a photodetector capable of operating over broad spectrum is invaluable to cope with many scenarios such as unmanned vehicle, military reconnaissance and target tracking.[2–4] However, commercial broadband photodetecting technique usually requires external power supply to implement the devices, and the combination of materials with dipartite bandgaps like Ga_2O_3, Si, HgCdTe to match the separated spectral branches would lead to demerits in circuit design and integration.[5–8] Exploring a suitable strategy to realize a self-driven broadband photodetector with low power consumption, therefore, has become an insistent need to meet the increasing demands. Owing to their considerable light-matter interaction and super integration, two-dimensional (2D) materials have been granted great potential for self-driven broadband photodetectors.[9–12] Unfortunately, the self-driven broadband photodetectors based on 2D materials are usually working in visible spectrum, which hampers their further applications in biomedicine, night driving, gas detection and other fields where infrared spectrum detection is necessary.[13] Indeed, narrow-bandgap 2D materials such as black phosphorus (BP), black arsenic (b-As), and tellurium (Te) are of interest to researchers because they allow the photodetectors to extend their detection range further into the infrared spectrum.[14–17] Therefore, the exploration of state-of-the-art self-driven broadband photodetectors covering from visible to infrared spectrum by implementing narrow-bandgap 2D materials will greatly simplify the detection system and bring great convenience in complex visual information processing.

Asymmetric contact strategy is widely applied for self-driven photodetectors with Schottky junction.[18] For the common 2D materials, Schottky barriers are usually established between metal electrodes and channel, and band bending occurs at their interface creating a strong electronic field due to the huge work function differences of metal electrodes. In this case, the separation of photo-generated carriers is determined by the electric field and produces a photovoltaic (PV) effect for self-driven photodetector. Interestingly, the sharp interface of 2D heterostructures has led some studies to turn their attention to the contact of 2D semimetals and layered channels.[19–22] For instance, an inherent potential barrier is observed at graphene-transitional metal dichalcogenides (Gr-TMDCs) interface, highlighting a novel strategy for constructing high-sensitivity Schottky photodetectors.[19,23–25] In addition, semimetal Gr can also be applied to construct ohmic contact with several TMDCs due to their close Fermi level. For example, perfect ohmic contact was

K. Tang, C. Yan, X. Du, G. Rao, M. Zhang, Y. Wang, X. Wang, J. Xiong
State Key Laboratory of Electronic Thin Films and Integrated Devices
University of Electronic Science and Technology of China
Chengdu 610054, China
E-mail: cyan@uestc.edu.cn; xfwang87@uestc.edu.cn; jiexiong@uestc.edu.cn

The ORCID identification number(s) for the author(s) of this article can be found under https://doi.org/10.1002/adom.202301350

DOI: 10.1002/adom.202301350

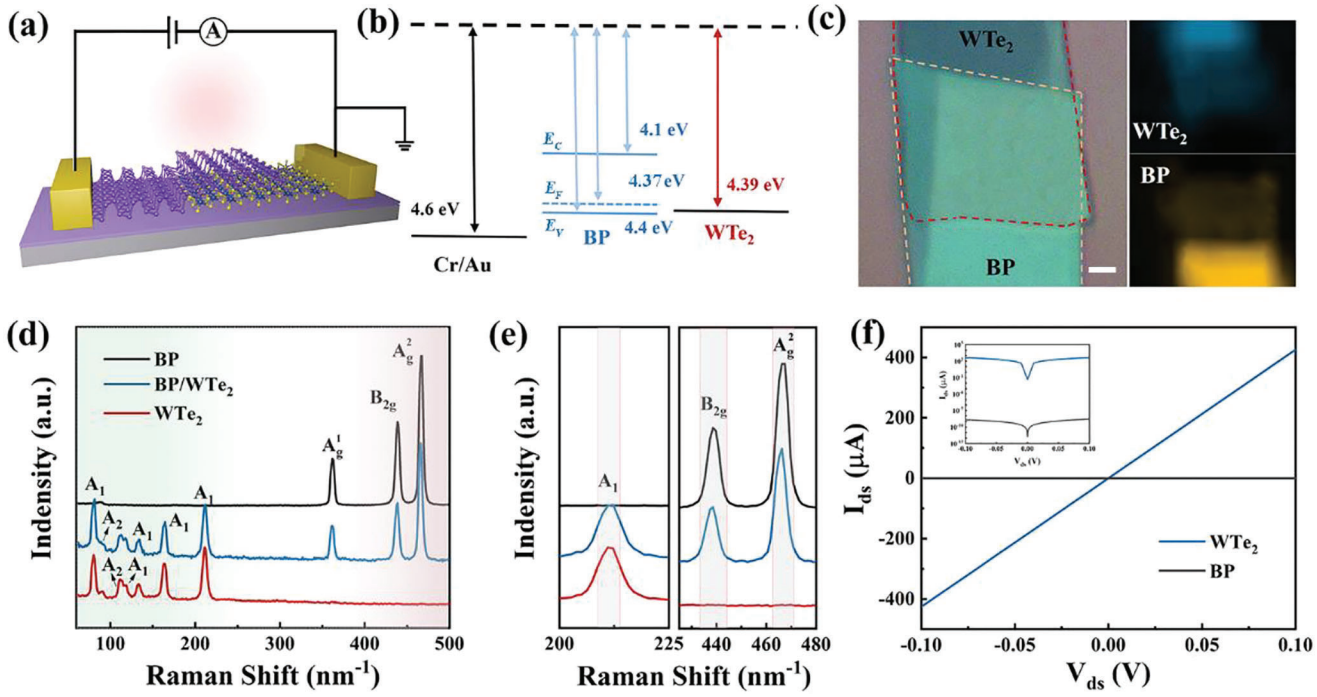

Figure 1. a) Schematic diagram of the self-driven broadband photodetector based on BP nanosheet with Cr and WTe_2 as electrodes. b) Band diagram before band alignment of Cr, BP and WTe_2. c) Optical image of BP/WTe_2 heterostructure and Raman mapping images of the A_1 mode for WTe_2 and the A_g^1 mode for BP, scale bar: 2 μm. d) Raman spectrum of BP, WTe_2 and BP/WTe_2 heterostructure. e) Raman shifts of the A_1 (212.2 eV), B_{2g} (436 eV), A^1_g (463 eV) peaks of WTe_2, BP and the heterostructure. f) The $I_{ds}-V_{ds}$ characteristics of the symmetric BP and WTe_2 devices.

formed at the Gr-InSe interface in the asymmetric Au/InSe/Gr heterostructure, which accelerates the rapid carrier transit to the Gr electrode, rendering an ultrafast and sensitive self-driven photodetector.[18] Furthermore, several 2D semimetals such as Mo_2C, $NiTe_2$, $NbTe_2$ and $PtTe_2$ have also been developed successively to achieve good ohmic contact with numerous 2D semiconductor channels for self-driven photodetectors.[26–29] Regrettably, these self-driven photodetectors with asymmetric contacts are usually based on large-bandgap TMDCs, which limits the detectable range in visible spectrum. Although narrow-bandgap 2D materials can extended the detection range to infrared spectrum, asymmetric contact with conventional metal electrodes makes it difficult to generate a strong potential barrier at the two ends of the channel. The combination of Schottky and ohmic contacts makes a better choice for narrow-bandgap 2D materials to fabricate self-driven broadband photodetector covering from visible to infrared spectrum, however, which has not yet been realized because the ideal ohmic contact is difficult to construct due to the band structure mismatch of the channel and metal electrodes.[30,31]

Herein, we report a self-driven broadband photodetector based on narrow-bandgap BP nanoflakes with detectable spectral range from visible to infrared spectrum by constructing good asymmetric Schottky and ohmic contacts at the Cr/BP/WTe_2 interfaces, where Cr metal and WTe_2 semimetal act as the electrodes. In the well-engineered band structures, the photo-generated holes are driven to the metal electrode owing to the self-limited depletion region induced by Schottky junction, and the electrons can flow rapidly to WTe_2 electrode, rendering the photodetector broadband response from 532 to 1550 nm without external potential supply. The broadband photoresponse of the self-driven photodetector is confirmed from 532 to 1550 nm, and the responsivity (R) is up to ~283 mA/W with corresponding detectivity (D^*) of ~2.3×10^{11} Jones under 532 nm illumination. The responsivity and the measured detectivity also remain higher than ~193 mA/W and ~1.2×10^{11} Jones, respectively, when illuminated by the incident light with a wavelength of 1550 nm. Due to the robust depletion region induced by the Schottky barrier, an ultralow dark current noise of ~10^{-13} A is observed contributing greatly to the high detectivity of BP broadband self-driven photodetector. Our results show that the well-designed band structure is suitable to construct ideal Schottky and ohmic contacts for narrow-bandgap 2D materials to realize self-driven broadband photodetectors from visible to infrared spectrum and can be used for wide-range multispectral imaging.

2. Results and Discussion

In order to enable a self-driven broadband photodetector to work in the infrared wavelengths, 2D BP with a narrow bandgap of 0.3 eV was chosen as the photosensitive medium. **Figure 1**a depicts the architecture of the self-driven BP broadband photodetector, in which the Cr/Au layer (5/50 nm) and a few-layered T_d-phase WTe_2 nanosheet are adopted as electrodes and expected to construct Schottky and ohmic contact with BP, respectively. Figure S1 shows the typical optical image of the device, where vertical BP/WTe_2 heterostructure is fabricated by mechanically exfoliating the crystals followed with being stacked on SiO_2/Si

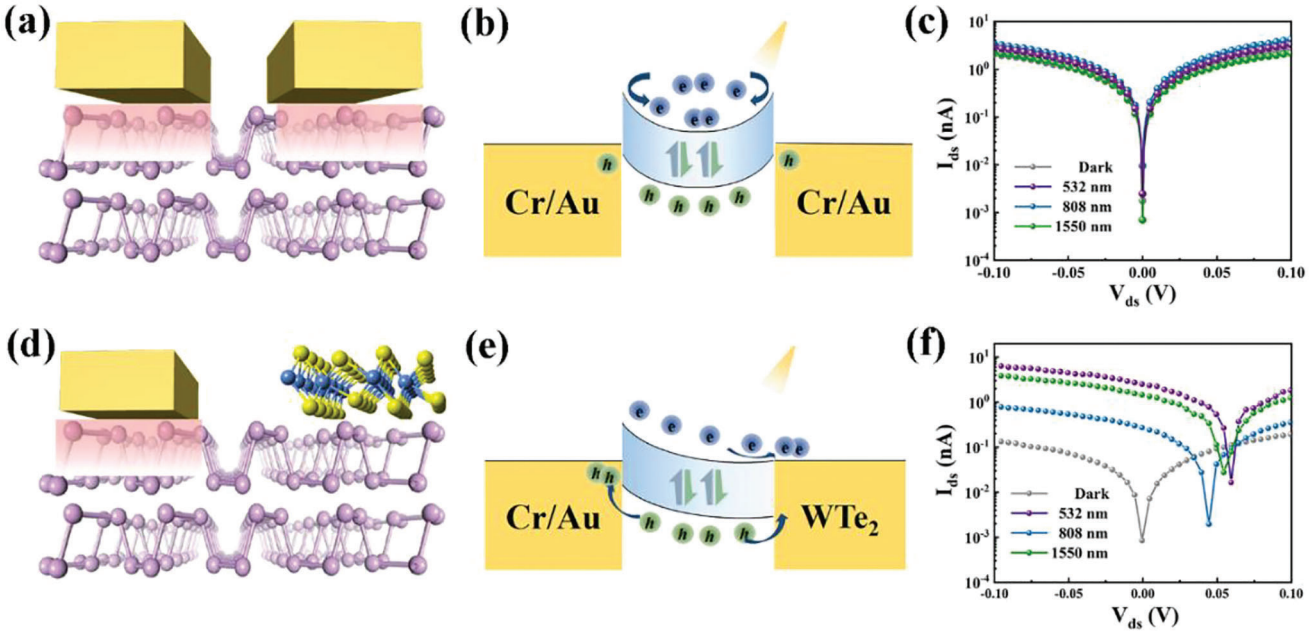

Figure 2. a,d) Device structures, b,e) energy band diagrams after band alignments and c,f) corresponding I_{ds}–V_{ds} characteristics as a function of different lasers of BP photodetectors with symmetric Cr/Au electrodes and asymmetric Cr/Au and WTe_2 electrodes, respectively. The power of the lasers is 5 nW.

substrate. To elaborate the asymmetric contacts, the work functions of Cr (4.6 eV) and WTe_2 (4.39 eV), and the Fermi level of BP (4.37 eV) are referred from the reported literatures.[32–34] The energy band diagram before the Fermi level equilibrium is illustrated in Figure 1b. Accordingly, owing to the huge difference in the band structure, a robust Schottky contact can be formed at the Cr-BP interface. Instead, a good ohmic contact can be formed between BP and WTe_2 layers owing to their nearly equal Fermi levels. Consequently, an asymmetric contact barrier is constructed at the two ends of BP channel driving the separation of photogenerated electron-hole pairs.

The Raman mappings of the BP/WTe_2 heterostructure are demonstrated in Figure 1c, homogeneously distributed A_1 mode at 216 cm^{-1} and A_g^1 mode at 360 cm^{-1} reveal the the smooth and clean interface between BP and WTe_2 layers. Meanwhile, an obvious Raman quenching effect occurs in overlapping area, exhibiting a photo-generated carrier recombination through a non-radiative way.[18,35,36] The crystalline quality and vibration modes of BP, WTe_2 and vdW heterostructure was confirmed by Raman spectroscopy under excitation of 532 nm laser (Figure 1d). In the WTe_2 region, seven peaks located at 85.3, 96.3, 111.6, 116.3, 133.4, 163.1, and 212.2 cm^{-1} are specified as the A_1, A_2, A_2, A_1, A_1, A_1, and A_1 phonon modes, respectively.[37,38] Three strong peaks located at 360, 436 and 463 cm^{-1} are observed in BP region, which are consistent with the results reported in the literatures.[39] It's worth noting that the Raman peaks of WTe_2 and BP in the overlapping region show a negligible shift behavior (Figure 1e), indicating the good interface quality in the heterostructure, which is conductive to the formation of ohmic contact at the interface.[40] In addition, to investigate the metallic behavior of WTe_2, pristine WTe_2 and BP devices with symmetric Cr/Au electrodes were fabricated on SiO_2/Si substrates, respectively. The output characteristic curve (I_{ds}–V_{ds}) of pristine BP device shows a current on ~nA level with the V_{ds} varying from −0.1 to 0.1 V, confirming the semiconducting properties of BP (Figure 1f). A symmetric and linear output characteristic curve and large current are observed in WTe_2 device, verifying the strong conductivity of T_d-phase WTe_2. Else, for the pristine WTe_2 device, the drain current is independent of the back-gate voltage as shown in the transfer characteristics (Figure S2), further proving that the selected T_d-phase WTe_2 can be used as metal electrodes. In addition, the BP device with symmetric WTe_2 electrodes is also prepared, and a very linear behavior is found in the output characteristic curve, confirming the ohmic contact between WTe_2 and BP (Figure S3).

Asymmetric contact with built-in electric fields for self-driven photodetector was achieved by manufacturing Schottky and ohmic contacts at the two ends of the BP channel, respectively. Initially, for comparison, the devices with symmetric and asymmetric structures (Cr/Au-BP-Cr/Au, Cr/Au-BP-WTe_2) were fabricated and measured as well (**Figure 2**a,d). The corresponding energy band diagrams are studied according to the equation: $\Phi_b = \Phi - \chi$, where Φ_b, Φ and χ represent the Schottky barrier, work function of the metal and the electron affinity of semiconductor, respectively. On account of the above band structure, a strong Schottky contact and a good ohmic contact would be formed at Cr-BP and WTe_2-BP interface, respectively. As a result, an energy barrier emerges due to band bending at the Cr-BP interface while it is absent at the WTe_2-BP interface. Thus, in symmetric BP device, a large number of photo-generated electrons are blocked by the high Schottky barrier and cannot be collected by external electrodes under zero bias (Figure 2b). Under light illumination, only a negligible photocurrent under zero bias (named short-circuit current, I_{sc}) can be achieved, and a bias voltage is usually required to change the energy band structure and produces a measurable photocurrent (Figure 2c). By contract, in the asymmetric BP de-

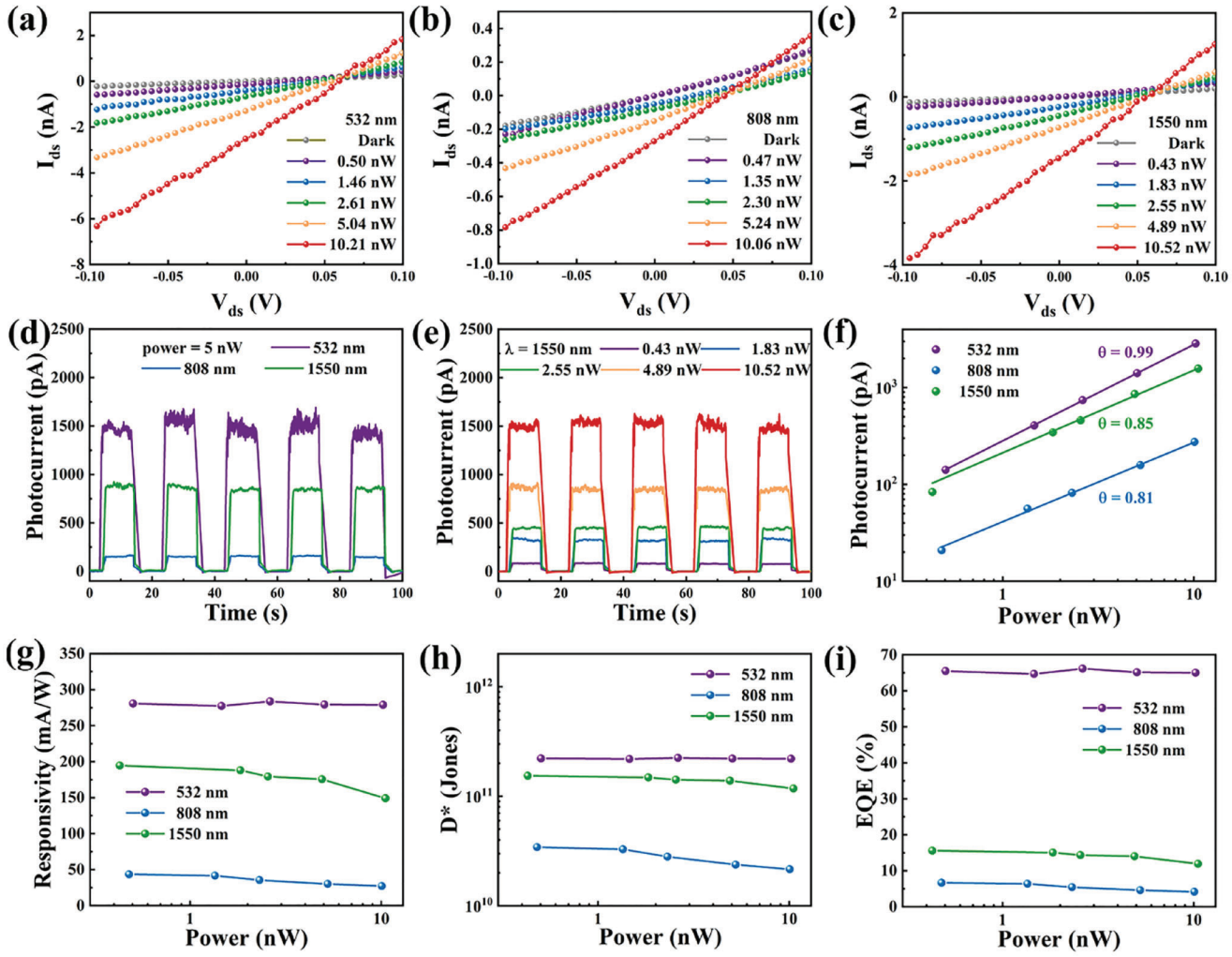

Figure 3. Photodetecting performances of the self-driven broadband photodetector. The I_{ds}-V_{ds} characteristics of the photodetector with variable light power intensity: a) 532 nm, b) 808 nm, and c) 1550 nm. d) The corresponding time-dependent photocurrent response under switched-on/off light illumination with 5 nW. e) Time-dependent photocurrent response under 1550 nm illumination with different power intensities. f) Fitted photocurrent, g) responsivity, h) detectivity, and i) EQEs of devices as a function of the illumination intensity of lasers with different wavelengths.

vice, after the Fermi levels are aligned, a band bending occurs at the Cr-BP interface because of the gap between the work function of Cr (4.6 eV) and the fermi level of BP (4.37 eV). Instead, no band bending occurs at the WTe_2-BP interface because the value of equal Fermi level of BP (4.37 eV) is close to that of the work function of WTe_2 (4.39 eV). Thus, in such an energy band structure, a unilateral built-in electric field is established. When the device is exposed to incident light, the photo-generated holes and electrons can be rapidly separated by the built-in electric field under zero bias (Figure 2e). Hence, a reliable and stable short-circuit currents are achieved under light illumination with various wavelengths, indicating the great potential of asymmetric BP device for self-driven broadband photodetector (Figure 2f).

The performance of asymmetric BP device was measured by illuminating lights with variable power, and the short-circuit currents were recorded to evaluate the self-driven photodetection capability of the device in a broadband spectrum from 532 to 1550 nm. As shown in **Figure 3**a, under 532 nm illumination, the drain-source current shows a dramatic increase, and significant short-circuit currents are observed which can reach the maximum value of 3.3 nA under 10.21 nW illumination, demonstrating the excellent photodetecting properties under zero bias. In addition, the asymmetric BP photodetector exhibits an ultralow dark current because of the large depletion region around Cr-BP interface (Figure S4). Therefore, an ultrahigh photoswitching ratio over 10^4 can be achieved for 532 nm wavelength under self-driven mode (Figure S5). Because of the weak light absorption of BP for 808 nm wavelength, relatively low photocurrent is generated within this wavelength (Figure 3b). When the wavelength of incident light is extended to infrared 1550 nm, a significant increase in photocurrent is detected again (Figure 3c), which can be attributed to the photon energy in the infrared band being closer to the band gap absorption of BP. Figure 3d shows the time-resolved photoresponse of the self-driven broadband photodetector under light illumination with various wavelengths. As demonstrated, the photodetector can be switched reversibly

with good stability and reproducibility along with the continuous switching of the laser. In addition, the photocurrents of the device under light illumination of 532 and 1550 nm laser with power of 5 nW are much higher than that of device at the incident wavelength of 808 nm, corresponding well with the above results. Figure 3e shows the time-resolved responses under infrared 1550 nm illumination with various light powers. It can be seen that the self-driven broadband photodetector shows the ability of free switching for infrared 1550 nm in a wide power range. The rapid photoresponse reveals that the photocurrent of the self-driven photodetector under broadband incident light illumination is generated by the photovoltaic effect rather than the thermoelectric or radiant heat effect. It is worth noting that the photocurrent expressed here is actually negative. For convenience, the photocurrent values here are treated as their absolute values.

In order to quantitatively evaluate the photodetection performance of the self-driven broadband photodetector, key quality factors including responsivity (R) and specific detectivity (D*) were calculated. Figure 3f–i depicts the variation trend of photocurrent, responsivity, detectivity and external quantum efficiency (EQE) under laser illumination of 532, 808 and 1550 nm with various powers. To investigate the light power dependence of self-driven photocurrent, the power-law relation $I_{ph} \propto P^{\alpha}$ was used to fit the experimental datas.[41] For an ideal photovoltaic device, the photocurrent theoretically depends linearly on the power density of incident light, where $\alpha = 1$ in the power-law relation. In the range of light powers, the photocurrent (Figure 3f) exhibits a very linear relationship with the incident light power, and the value of index α is 0.99, 0.85 and 0.81 for 532, 1550 and 808 nm illumination, respectively, indicating that the self-driven broadband photodetector has excellent linear response for broadband wavelengths without external power supply. Since photocurrent is linearly correlated with incident light power, responsivity can be expected to be constant. As can be seen from Figure 3g, under zero bias, responsivity has little change in the whole range of the light powers. It is worth noting here that the constant responsivity can be regarded as one of the characteristic attributes of photovoltaic effect. The responsivity can reach 283 and 193 mA/W under 532 and 1550 nm illumination, respectively, due to the large number of photo-generated carriers being separated, which can be comparable to that of the most reported Schottky photodetector based on 2D semiconductors. Furthermore, the normalized responsivity with the incident light wavelength of 500–1550 nm is shown in Figure S6. The peak response can be observed at the excitation wavelength of ~680 and ~1400 nm, and the overall trend is consistent with the results under separated wavelengths.

Detectivity is another key parameter that can be used to evaluate the sensitivity of photodetectors for weak signals. When the dark current is the major occupation of noise floor, detectivity can be calculated according to the formula: $D^* = RA^{1/2}/(2qI_{dark})^{1/2}$, where A, q, I_{dark} represent the effective area, electronic charge and dark current, respectively.[9] Similar to responsivity, detectivity presents power-independency, and the corresponding values of approximately 2.3×10^{11}, 3.50×10^{10}, and 1.2×10^{11} Jones are obtained at 532, 808, and 1550 nm wavelengths, respectively (Figure 3h). In addition, EQE is the ratio of the number of charge carriers in the photocurrent n_e and the total number of incident photons n_p, and can be used to better explore the intrinsic photoresponse. EQEs of the self-driven broadband photodetector under zero bias were calculated according to the formula: EQE = $n_e/n_p = R_\lambda hc/q\lambda$, where h is Planck's constant, c is the speed of light in vacuum, q is the electronic charge, and λ is the photon wavelength. It can be found that EQE of the self-driven broadband photodetector is 67% in visible region ($\lambda = 532$ nm), while EQEs decrease to 8% and 15% at 808 and 1550 nm wavelengths, which are much larger than that of other self-driven 2D Schottky photodetectors.

The spatially resolved photocurrent map of the self-driven broadband photodetector was collected to study the photoresponse mechanism under zero bias. During spot scanning using a 1550 nm focused laser, the short-circuit current is recorded as a function of position (**Figure 4**a). The photocurrent mapping image exhibits that the photocurrent originates around the Cr-BP contact edge, proving the photovoltaic effect generated from the Schottky contact at Cr-BP interface and a good ohmic contact at BP-WTe_2 interface. The same result is observed under 520 nm illumination, which exhibits a brighter response around the metal electrode owing to the higher incident photon energy (Figure S7). Considering the optoelectronic mechanism induced by the Schottky junction at the Cr-BP contact edge, it is necessary to simulate the potential distribution in the asymmetric self-driven photodetector. Figure 4b and Figure S8 show the different views of the potential distribution for the self-driven broadband photodetector. A depletion region with a potential gradient is observed near Cr-BP interface due to the unequal distribution of electrons and holes. The lateral depletion region drives the rapid separation and transfer of photo-generated carriers, which matches well with the band structure mechanism and scanning photocurrent mapping results. Considering the above results, it can be concluded that the large lateral depletion region practically dominates the photoresponse in the self-driven broadband photodetector.

As is well known, infrared detection depends largely on the working temperature, as loud noise will be produced due to the high energy electrons induced by temperature which inevitably confuse the true photocurrent. Therefore, low working temperatures can be expected to favor infrared detection. Figure 4c depicts the time-resolved photocurrents of the self-driven photodetector for 1550 nm wavelength at 198, 248 and 298 K, respectively, and increased infrared photoresponse is discovered at lower working temperature. The sensitivity for the device grows with the decrease of working temperature (Figure 4d), as the R value (637 mA/W) at 198 K are nearly 3.5 times higher than that measured at room temperature. Therefore, it can be inferred that low-temperature working conditions can greatly improve the photoresponse of the self-driven broadband photodetector, bringing it closer to the criterion of commercial infrared photodetectors.

Furthermore, the height of Schottky barrier is one of the decisive factors affecting photoresponse. The extra bias can strongly change the Schottky barrier and accelerate the separation of photo-generated carriers. Figure 4e shows the dependence of photocurrent on various bias voltages under illumination of 1550 nm with 4.89 nW. As demonstrated, the direction of the photocurrent is opposite when the open-circuit voltage changed from positive to negative. Furthermore, from Figure 4f, it can be seen that the responsivity of the photodetector under negative bias are obviously superior to those at positive bias. The results are consistent with the behaviors of optoelectronic devices with

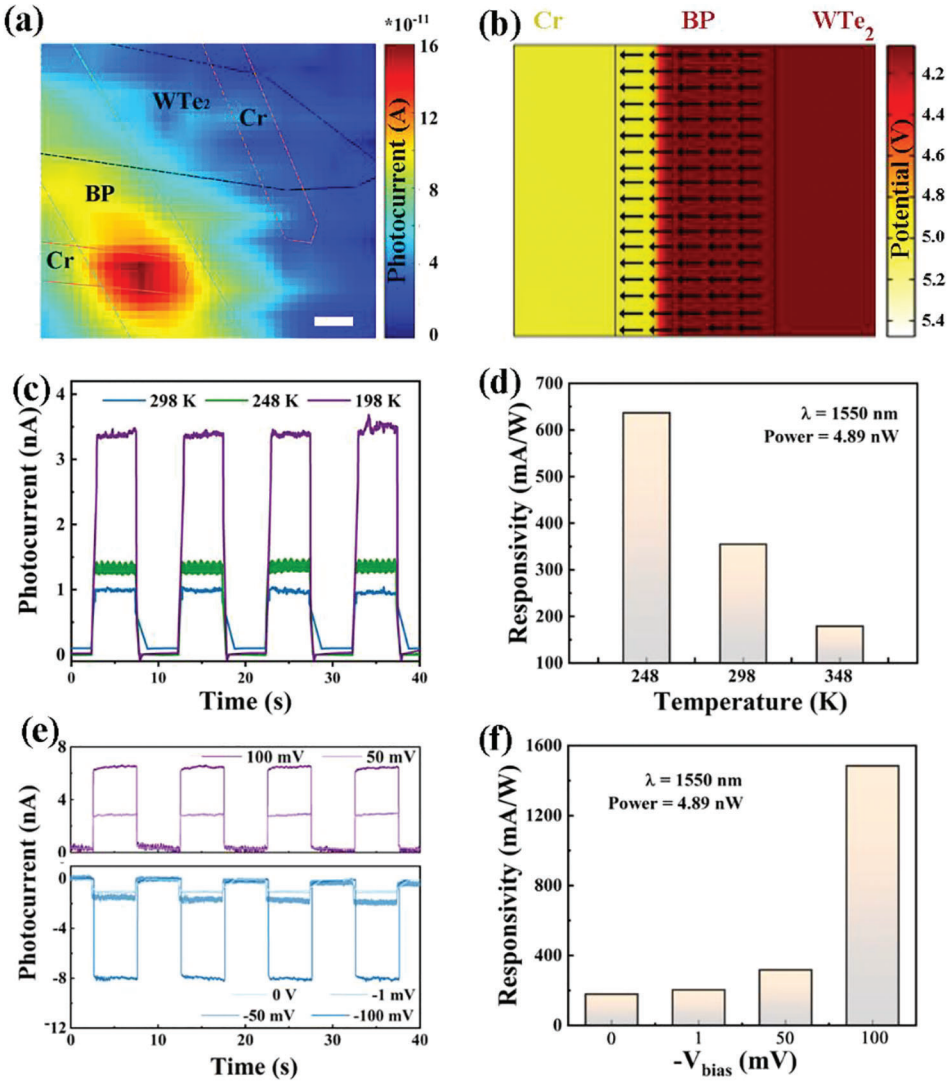

Figure 4. a) Scanning photocurrent mapping of the device under 1550 nm laser illumination with the laser spot size of ~2 μm at V_{ds} = 0 V, scale bar: 2 μm. b) Simulated lateral potential distribution of the device under zero bias. c) Time-dependent photocurrent response under switched-on/off light illumination and d) responsivity of the device under different working temperatures, the laser wavelength is 1550 nm. e) Time-dependent photocurrent response under switched-on/off light illumination and f) responsivity of the device under different biases.

Schottky junction, which implies that the self-driven broadband photodetector operates mainly at the photovoltaic mode. At a bias of -100 mV, the responsivity can be further enhanced to 1484 mA/W, about 8.3 times higher the value measured under zero bias.

Given the prominent photosensitivity in infrared region, it can be expected that the self-driven broadband photodetector demonstrates outstanding potential in infrared image sensing. In order to prove its feasibility in practical optical applications, we explored the infrared imaging capability of the self-driven broadband photodetector. **Figure 5**a shows the schematic diagram of imaging system for a single pixel imaging measurement. With the movement of mask, the position-resolved photocurrent was recorded sequentially. The self-driven broadband photodetector can work well at room temperature, which is expected to solve the bottleneck of existing power consumption and operating temperature problems for future scientific and industrial applications. A 5×5 array device was prepared on the Si/SiO_2 substrate. Because of the randomness of the exfoliated 2D material, the size and distribution of the pixels are not uniform. The preparation of perfect array devices based on 2D materials depends on the large-area synthesis and etching technology of 2D materials, which is still a challenge to be solved. Therefore, a mask of demo letters "UESTC" are designed and used to irradiate the array device in sequence (Figure 5b) to evaluate its potential application in an integrated light detection system. By moving the mask to control whether each pixel is irradiated by 1550 nm light, and the photocurrent and the dark current are recorded from pixels under the exposed area and the shaded area, respectively. Photocurrent imaging is shown in Figure 5c–h, and these results confirm that the self-driven broadband photodetector exhibits great potential in infrared imaging applications.

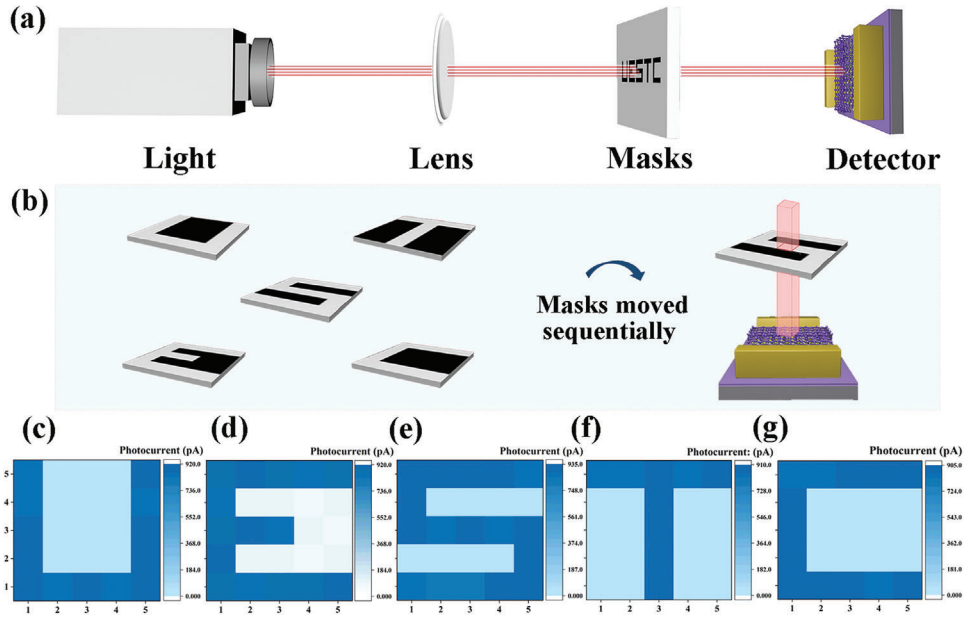

Figure 5. The imaging sensing application of the asymmetric self-driven broadband photodetector. (a) Schematic diagram of imaging system at zero bias under 1550 nm. (b) Schematic diagram of metal masks and experimental operation. c–g) Imaging results of letters (UESTC) with 5×5 pixels under 1550 nm illumination.

3. Conclusion

In summary, we designed a good asymmetric Schottky and ohmic contacts in the Cr/BP/WTe_2 heterostructure by well-designing the band structure to realize self-driven photodetector with outstanding broadband photodetection performance for visible to infrared spectrum. The self-driven broadband photodetector shows a sensitive responsivity of ~283 mA/W and detectivity of ~2.3×10^{11} Jones under 532 nm illumination, and remains ~193 mA/W and ~1.2×10^{11} Jones when illuminated by 1550 nm laser under zero bias at room temperature, due to the asymmetric contact barrier formed at the two ends of BP channel driving the fast separation of photo-generated electron-hole pairs. Our results show that the well-designed band structure contributes to constructing good Schottky and ohmic contact on narrow-bandgap 2D materials, and the as-fabricated self-driven photodetector can achieve great optoelectronic performance covering a broadband spectrum. These findings highlight a simple and novel strategy for constructing predesigned band structure for further electronic and optoelectronic applications.

4. Experimental Section

Sample Fabrication: The self-driven broadband photodetectors are constructed based on BP/WTe_2 heterostructure, and a wet transfer technique is used to vertically stacked BP and WTe_2 nanoflakes exfoliated from bulk crystals with PDMS in a glove box filled with argon gas (Shanghai Onway Technology Co., Ltd.). WTe_2 nanoflakes with thickness of ~10 nm was first stacked on Si/SiO_2 as the bottom electrode. Then the BP nanoflakes with a thickness ~ 15 nm was exfoliated on a flexible PPC substrate coated with a PDMS thin film. The selected BP nanoflakes were transferred onto WTe_2 nanoflake by utilizing optical microscopy and a homemade alignment transfer system. Finally, two Cr/Au electrodes were fabricated by the electron beam exposure and thermal evaporation techniques.

Device Characterization: The structure of the self-driven broadband photodetector was observed using an optical microscope (Olympus BX41). Raman spectra and mappings were measured via utilizing a Horiba micro-Raman system (Labraxm HR Evolution) with 532 nm laser excitation. The electric and optoelectronic performances were studied on the semiconductor parameter analyzer (Keithley, 4200-PA SCS). In our work, the effective area of the device was identified as the BP region between the Cr/Au and WTe_2 electrodes, and this area and the power density of the laser are used to calculate the responsivity. Detectivity can be calculated according to the formula: $D^* = RA^{1/2}/(2qI_{dark})^{1/2}$, where A, q, I_{dark} represent the effective area, electronic charge and dark current, respectively. EQEs of the self-driven broadband photodetector under zero bias were calculated according to the formula: EQE $= n_e/n_p = R_\lambda hc/q\lambda$, where h is Planck's constant, c is the speed of light in vacuum, q is the electronic charge, and λ is the photon wavelength. A dark probe station (Lakeshore) was used to reduce the light interference from the external environment during the tests. The scanning photocurrent mappings were performed using a modulated laser beam (520 nm with a frequency of 100 Hz and 1550 nm with a frequency of 100 Hz) scanning over the device utilizing a scanning micromotion platform (Thorlabs GVS212). The lock-in technique (Signal Recovery model 7270) was employed to amplify the obtained photocurrent signals. The light power density was measured using a power meter (OPHIR, VEGA ROHS). The finite element method (FEM) with COMSOL Multiphysics software was used to model heterostructure devices in three-dimensional space, and spatial potential distributions in the device were simulated according to the electrical parameters of electrodes and semiconductors.

Supporting Information

Supporting Information is available from the Wiley Online Library or from the author.

Acknowledgements

We gratefully acknowledge the support from the National Natural Science Foundation of China (U20A20244, 52222206, 51972041, and

52102156), the National Key Research and Development Program of China (2021YFA0718800), and the Sichuan Science and Technology Program (2021JDTD0010).

Conflict of Interest

The authors declare no conflict of interest.

Data Availability Statement

The data that support the findings of this study are available from the corresponding author upon reasonable request.

Keywords

asymmetric contacts, black phosphorus, broadband photodetection, narrow bandgap, self-driven photodetectors

Received: June 8, 2023
Revised: July 31, 2023
Published online: September 4, 2023

[1] Z. Li, W. Ran, Y. Yan, L. Li, Z. Lou, G. Shen, *InfoMat* **2022**, *4*, 12261.
[2] X. Yu, P. Yu, D. Wu, B. Singh, Q. Zeng, H. Lin, W. Zhou, J. Lin, K. Suenaga, Z. Liu, Q. J. Wang, *Nat. Commun.* **2018**, *9*, 1545.
[3] Y. Yang, K. Zhang, L. Zhang, G. Hong, C. Chen, H. Jing, J. Lu, P. Wang, X. Chen, L. Wang, H. Xu, *InfoMat* **2021**, *3*, 705.
[4] Q. Liang, Q. Wang, Q. Zhang, J. Wei, S. X. Lim, R. Zhu, J. Hu, W. Wei, C. Lee, C. Sow, W. Zhang, A. T. S. Wee, *Adv. Mater.* **2019**, *31*, 1807609.
[5] Y. Lu, Z. Zhang, X. Yang, G. He, C. Lin, X. Chen, J. Zang, W. Zhao, Y. Chen, L. Zhang, Y. Li, C. Shan, *Nano Res.* **2022**, *15*, 7631.
[6] W. Tian, H. Sun, L. Chen, P. Wangyang, X. Chen, J. Xiong, L. Li, *InfoMat* **2019**, *1*, 140.
[7] D. Hu, Y. Wang, Y. Wang, W. Huan, X. Dong, J. Yin, *Mater. Lett.* **2022**, *312*, 131653.
[8] Q. Xu, I. T. Cheong, L. Meng, J. G. C. Veinot, X. Wang, *ACS Nano* **2021**, *15*, 18429.
[9] J. Li, Z. Wang, Y. Wen, J. Chu, L. Yin, R. Cheng, L. Lei, P. He, C. Jiang, L. Feng, J. He, *Adv. Funct. Mater.* **2018**, *28*, 1706437.
[10] X. Zhou, X. Hu, J. Yu, S. Liu, Z. Shu, Q. Zhang, H. Li, Y. Ma, H. Xu, T. Zhai, *Adv. Funct. Mater.* **2018**, *28*, 1706587.
[11] D. Wu, J. Guo, J. Du, C. Xia, L. Zeng, Y. Tian, Z. Shi, Y. Tian, X. J. Li, Y. H. Tsang, J. Jie, *ACS Nano* **2019**, *13*, 9907.
[12] W. Cheng, W. Tian, F. Cao, L. Li, *InfoMat* **2022**, *4*, e12348.
[13] L. Peng, L. Liu, S. Du, S. C. Bodepudi, L. Li, W. Liu, R. Lai, X. Cao, W. Fang, Y. Liu, X. Liu, J. Lv, M. Abid, J. Liu, S. Jin, K. Wu, M.-L. Lin, X. Cong, P.-H. Tan, H. Zhu, Q. Xiong, X. Wang, W. Hu, X. Duan, B. Yu, Z. Xu, Y. Xu, C. Gao, *InfoMat* **2022**, *4*, e12309.
[14] J. Tao, J. Jiang, S. Zhao, Y. Zhang, X. Li, X. Fang, P. Wang, W. Hu, Y. H. Lee, H.-L. Lu, D.-W. Zhang, *ACS Nano* **2021**, *15*, 3241.
[15] J. Yao, G. Yang, *Small* **2018**, *14*, 1704524.
[16] L. Tong, X. Huang, P. Wang, L. Ye, M. Peng, L. An, Q. Sun, Y. Zhang, G. Yang, Z. Li, F. Zhong, F. Wang, Y. Wang, M. Motlag, W. Wu, G. J. Cheng, W. Hu, *Nat. Commun.* **2020**, *11*, 2308.
[17] F. Wu, H. Xia, H. Sun, J. Zhang, F. Gong, Z. Wang, L. Chen, P. Wang, M. Long, X. Wu, J. Wang, W. Ren, X. Chen, W. Lu, W. Hu, *Adv. Funct. Mater.* **2019**, *29*, 1900314.
[18] M. Dai, H. Chen, F. Wang, M. Long, H. Shang, Y. Hu, W. Li, C. Ge, J. Zhang, T. Zhai, Y. Fu, P. Hu, *ACS Nano* **2020**, *14*, 9098.
[19] W. J. Yu, Q. A. Vu, H. Oh, H. G. Nam, H. Zhou, S. Cha, J.-Y. Kim, A. Carvalho, M. Jeong, H. Choi, A. H. Castro Neto, Y. H. Lee, X. Duan, *Nat. Commun.* **2016**, *7*, 13278.
[20] J. D. Mehew, S. Unal, E. Torres Alonso, G. F. Jones, S. Fadhil Ramadhan, M. F. Craciun, S. Russo, *Adv. Mater.* **2017**, *29*, 1700222.
[21] H. Xu, X. Han, X. Dai, W. Liu, J. Wu, J. Zhu, D. Kim, G. Zou, K. A. Sablon, A. Sergeev, Z. Guo, H. Liu, *Adv. Mater.* **2018**, *30*, 1706561.
[22] Z. Hu, X. Liu, P. L. Hernández-Martínez, S. Zhang, P. Gu, W. Du, W. Xu, H. V. Demir, H. Liu, Q. Xiong, InfoMat **2022**, *4*, e12290.
[23] W. Yu, Z. Dong, H. Mu, G. Ren, X. He, X. Li, S. Lin, K. Zhang, Q. Bao, S. Mokkapati, *ACS Nano* **2022**, *16*, 12922.
[24] H. Tan, Y. Fan, Y. Zhou, Q. Chen, W. Xu, J. H. Warner, *ACS Nano* **2016**, *10*, 7866.
[25] J. Lu, Z. Zheng, J. Yao, W. Gao, Y. Zhao, Y. Xiao, J. Li, *Small* **2019**, *15*, 1904912.
[26] X. Zhai, X. Xu, J. Peng, F. Jing, Q. Zhang, H. Liu, Z. Hu, *ACS Appl. Mater. Interfaces* **2020**, *12*, 24093.
[27] Z. Qi, X. Zhai, X. Jiang, X. Xu, C. Fan, L. Shen, Q. Xiao, S. Jiang, Q. Deng, H. Liu, F. Jing, Q. Zhang, *ACS Appl. Mater. Interfaces* **2022**, *14*, 31121.
[28] D. A. Nguyen, D. Y. Park, J. Lee, N. T. Duong, C. Park, D. H. Nguyen, T. S. Le, D. Suh, H. Yang, M. S. Jeong, *Nano Energy* **2021**, *86*, 106049.
[29] Z. Kang, Y. Cheng, Z. Zheng, F. Cheng, Z. Chen, L. Li, X. Tan, L. Xiong, T. Zhai, Y. Gao, *Nano-Micro Lett.* **2019**, *11*, 34.
[30] T. Chang, P. Chen, J. Yan, W. Li, Y. Zhang, D. Luo, J. Li, K. Huang, C. Liu, *ACS Appl. Mater. Interfaces* **2020**, *12*, 1201.
[31] J. Xu, Y. J. Song, J.-H. Park, S. Lee, *Solid-State Electron.* **2018**, *144*, 86.
[32] E. Torun, H. Sahin, S. Cahangirov, A. Rubio, F. M. Peeters, *J. Appl. Phys.* **2016**, *119*, 074307.
[33] J. R. Hajzus, A. J. Biacchi, S. T. Le, C. A. Richter, A. R. Hight Walker, L. M. Porter, *Nanoscale* **2018**, *10*, 319.
[34] L. Huang, J. Li, *Appl. Phys. Lett.* **2016**, *108*, 083101.
[35] F. Wang, Z. Wang, K. Xu, F. Wang, Q. Wang, Y. Huang, L. Yin, J. He, *Nano Lett.* **2015**, *15*, 7558.
[36] H. Wu, Z. Kang, Z. Zhang, Z. Zhang, H. Si, Q. Liao, S. Zhang, J. Wu, X. Zhang, Y. Zhang, *Adv. Funct. Mater.* **2018**, *28*, 1802015.
[37] Q. Song, X. Pan, H. Wang, K. Zhang, Q. Tan, P. Li, Y. Wan, Y. Wang, X. Xu, M. Lin, X. Wan, F. Song, L. Dai, *Sci. Rep.* **2016**, *6*, 29254.
[38] C.-H. Lee, E. C. Silva, L. Calderin, M. A. T. Nguyen, M. J. Hollander, B. Bersch, T. E. Mallouk, J. A. Robinson, *Sci. Rep.* **2015**, *5*, 10013.
[39] J. Miao, B. Song, Q. Li, L. Cai, S. Zhang, W. Hu, L. Dong, C. Wang, *ACS Nano* **2017**, *11*, 6048.
[40] L. Wang, X. Zou, J. Lin, J. Jiang, Y. Liu, X. Liu, X. Zhao, Y. F. Liu, J. C. Ho, L. Liao, *ACS Nano* **2019**, *13*, 4804.
[41] Y. Zhang, K. Ma, C. Zhao, W. Hong, C. Nie, Z. Qiu, S. Wang, *ACS Nano* **2021**, *15*, 4405.